

Maximizing the performance of n-type Mg_3Bi_2 based materials for room-temperature power generation and thermoelectric cooling

Zihang Liu^{1,4}, Weihong Gao^{1,4}, Hironori Oshima², Kazuo Nagase², Chul-Ho Lee ² & Takao Mori ^{1,3}✉

Although the thermoelectric effect was discovered around 200 years ago, the main application in practice is thermoelectric cooling using the traditional Bi_2Te_3 . The related studies of new and efficient room-temperature thermoelectric materials and modules have, however, not come to fruition yet. In this work, the electronic properties of n-type $\text{Mg}_{3.2}\text{Bi}_{1.5}\text{Sb}_{0.5}$ material are maximized via delicate microstructural design with the aim of eliminating the thermal grain boundary resistance, eventually leading to a high zT above 1 over a broad temperature range from 323 K to 423 K. Importantly, we further demonstrated a great breakthrough in the non- Bi_2Te_3 thermoelectric module, coupled with the high-performance p-type $\alpha\text{-MgAgSb}$, for room-temperature power generation and thermoelectric cooling. A high conversion efficiency of ~2.8% at the temperature difference of 95 K and a maximum temperature difference of 56.5 K are experimentally achieved. If the interfacial contact resistance is further reduced, our non- Bi_2Te_3 module may rival the long-standing champion commercial Bi_2Te_3 system. Overall, this work represents a substantial step towards the real thermoelectric application using non- Bi_2Te_3 materials and devices.

¹International Center for Materials Nanoarchitectonics (WPI-MANA), National Institute for Materials Science (NIMS), Tsukuba, Japan. ²National Institute of Advanced Industrial Science and Technology (AIST), Tsukuba, Ibaraki, Japan. ³Graduate School of Pure and Applied Sciences, University of Tsukuba, Tsukuba, Japan. ⁴These authors contributed equally: Zihang Liu, Weihong Gao. ✉email: MORI.Takao@nims.go.jp

The long-term climate policy, an economy with net-zero greenhouse gas emissions by 2050, is significantly affecting the global economic situation, which stimulates the rapid development of clean and sustainable energy-related technologies¹. Among them, thermoelectric effect can directly convert the temperature gradient to electricity and vice-versa. Despite the relatively low performance, thermoelectric devices have these unique advantages, including high reliability and scalability, no pollution and no noise, precise temperature control, enabling them suitable for a range of potential applications, such as aerospace power, refrigeration, and even energy harvesting^{2–7}. The corresponding thermoelectric conversion efficiency or the cooling coefficient of performance (COP) is mainly determined by the dimensionless thermoelectric figure of merit (zT), which is defined as $zT = [S^2\sigma/(\kappa_{lat} + \kappa_{ele})]T$, where S , σ , κ_{lat} , κ_{ele} , and T are Seebeck coefficient, electrical conductivity, lattice thermal conductivity, electronic thermal conductivity, and absolute temperature, respectively.

In general, the material's thermoelectric performance is dominated by its crystal structure, specific composition, as well as nano-microstructure. Despite the intertwined relationship, the rational compromise and synergy among these abovementioned factors enable the realization of a maximum zT for a given material^{8,9}. Previous investigations mainly focused on the modification of electronic band structure by elements alloying and/or tuning the phonon-scattering mechanism by designing special microstructure^{10–16}. Very recently, the significance of grain-boundary resistance on the low-temperature charge transport has been recognized in some material systems^{17–19}. This frequently overlooked effect leads to a lower charge carrier mobility and deteriorated practical zTs compared to their predicted values.

Bi_2Te_3 related alloys, which are discovered around the 1950 s as the best room-temperature thermoelectric material, are used in the commercial cooling area^{20,21}. However, one of the main reasons that limit its further wide applications is the scarcity of Tellurium (Te) element. During the past decade, some new Te-free thermoelectric candidates with high zTs , such as $\alpha\text{-MgAgSb}$ ^{22–24}, Mg_3Bi_2 ^{25–30}, SnSe ^{31,32}, enable the potential replacement of Bi_2Te_3 , in which a high power-generation performance of $\text{Mg}_3\text{Sb}_2/\text{MgAgSb}$ module, with the target for harvesting low-temperature waste heat, has already been demonstrated very recently^{33,34}. P-type $\alpha\text{-MgAgSb}$ shows the large enhancement of thermoelectric performance at the low-temperature range by suitable doping^{22,35}. Alloying with Mg_3Bi_2 in n-type Mg_3Sb_2 yields the optimum bandgap and simultaneously strengthens the point-defect scattering^{25–28,36–45}, therefore contributing to highly competitive zTs . Moreover, a high-performance uni-couple (with p-type $\text{Bi}_{0.5}\text{Sb}_{1.5}\text{Te}_3$) for thermoelectric cooling has been experimentally realized²⁵. However, there is still no report about non- Bi_2Te_3 Peltier module thus far, due to a combination of the complicated synthesis method and the challenging module-fabrication process for these non- Bi_2Te_3 thermoelectric systems. Very recently, thermoelectric module consisting of n-type Bi_2Te_3 and p-type SnSe showed a maximum temperature difference ΔT_{max} of 45.7 K³², being attractive for future applications.

Herein, the thermoelectric performance of $\text{Mg}_3(\text{Bi}, \text{Sb})_2$ system was fully maximized through rational microstructural design to eliminate the intrinsic grain-boundary resistance, which contributed to a higher zT than the commercial n-type Bi_2Te_3 above room temperature (Fig. 1a). Coupled with the optimized p-type $\alpha\text{-MgAgSb}$ (Fig. 1a), we demonstrated a remarkably high thermoelectric performance of non- Bi_2Te_3 and 8-pairs module for room-temperature power generation and thermoelectric cooling. These images of both the fabricated module and the cooling-performance measurement setup were given here (Fig. 1b). Specifically, at the ΔT of 35 K, the η and the maximum output

power P_{max} reached 0.95% and 0.016 W (Fig. 1c), respectively. Moreover, the peak η reached 2.8% associated with a P_{max} of 0.12 W at the ΔT of 95 K. The calculated output power density of our fabricated module, with a whole cross-sectional dimension of 18 mm \times 15 mm, was comparable to the zone-melting Bi_2Te_3 module (Fig. S1)⁴⁶. Meanwhile, for cooling applications, when working at the optimum electric current I with a hot-side temperature T_h of 323 K, the ΔT_{max} and the maximum cooling power P_{max} could reach 56.5 K and 3.0 W (Fig. 1d), respectively. The achieved thermoelectric performance of our fabricated module is higher than the recently reported high-performance $\text{SnSe}/\text{Bi}_2\text{Te}_3$ module³², even comparable to the commercial Bi_2Te_3 ^{46,47} (Fig. 1e). Considering the billion-US-dollar market for the global thermoelectric Peltier module, this work brings promise for non- Bi_2Te_3 thermoelectric cooling and therefore paves up the avenue for emerging cooling technology.

Results and discussion

To possess the optimum bandgap for the room-temperature application, it is imperative to shift the target material of $\text{Mg}_3(\text{Bi}, \text{Sb})_2$ system from Sb rich to Bi rich. Hence, $\text{Mg}_3\text{Bi}_{1.5}\text{Sb}_{0.5}$ is chosen as the basic composition, and doping with a little Te enables to tune the carrier concentration. Since minor Cu addition in $\text{Mg}_3\text{Sb}_{1.5}\text{Bi}_{0.5}$ realized the remarkable enhancement of low-temperature zT ³³, herein the nominal composition is $\text{Mg}_{3.2}\text{Bi}_{1.5}\text{Sb}_{0.48}\text{Te}_{0.002}\text{Cu}_{0.01}$. We revealed that the spark plasma sintering (SPS) temperature has a noticeable impact on the thermoelectric properties, which is beyond the conventional understanding that sintering temperature only affects the densification mechanism or main-phase change^{48,49}. The phase feature when sintered at the different temperatures was thoroughly investigated by a combination of X-ray diffraction (XRD) analysis, in situ SPS displacement record, and differential scanning calorimetry (DSC) measurement (Fig. 2). Apparently, no impurity phase can be observed for the sample sintered at 723 K (Fig. 2a). In contrast, Bi impurity phase starts to appear at a higher sintering temperature than 723 K (Fig. S2). Meanwhile, the significant evaporation and the appearance of the squeezed melting phase are observed simultaneously (Fig. S3). Furthermore, XRD pattern of the melting-phase reveals that it consists of two different phases (Fig. 2b), namely Bi and $\text{Mg}_3(\text{Bi}, \text{Sb})_2$. This should be related to the high-temperature decomposition of $\text{Mg}_3(\text{Bi}, \text{Sb})_2$ due to its intrinsic instability, which is revealed through synchrotron powder XRD measurements along with synchrotron X-ray total scattering during repeated thermal cycling of $\text{Mg}_3\text{Sb}_{1.475}\text{Bi}_{0.475}\text{Te}_{0.05}$ powder reported by Jørgensen et al.⁵⁰ This phenomenon can be further confirmed by the in situ recorded SPS displacement during the sintering process (Fig. 2c). For the sample sintered at 1073 K, there exist three independent plateaus that are distinct from other samples: the first one appears at the sintering-temperature range of 623–773 K, the second one during 843–1000 K, as well as the third one at the 1073 K isothermal process. These two melting phases are squeezed out during these abovementioned temperature ranges meanwhile Mg evaporation leads to the formation of nano-micro pores. As the utilization rate of raw materials is not 100%, the squeezed melting phase is associated with a little economic loss. For the heating DSC measurement (Fig. 2d), the exothermic peak at 858 K may be due to relaxing the lattice strain since the previous report claimed the origin of the crystalline Bi phase is caused by a reduction of microscopic strain in the structure⁵⁰, while the subsequent endothermic reaction should be related to the severe partial decomposition reaction.

In addition to the phase component, tuning the sintering-temperature affects the microstructural feature considerably. As

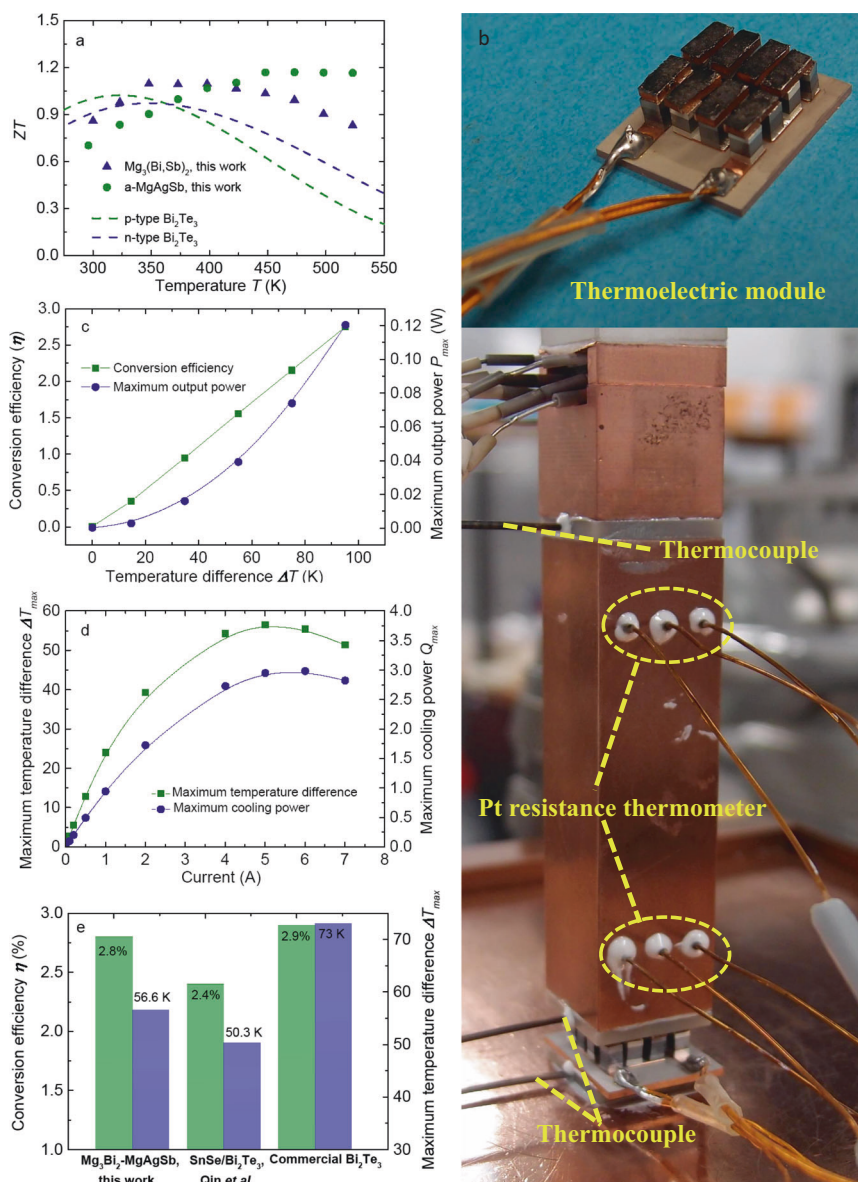


Fig. 1 High-performance thermoelectric module, consisting of n-type $\text{Mg}_{3.2}\text{Bi}_{1.5}\text{Sb}_{0.498}\text{Te}_{0.002}\text{Cu}_{0.01}$ and p-type $\alpha\text{-Mg}_{0.99}\text{Cu}_{0.01}\text{Ag}_{0.97}\text{Sb}_{0.99}$, for room-temperature power generation and cooling application. (a) Temperature-dependent zT of both n-type and p-type materials in comparison to commercial Bi_2Te_3 data⁸, (b) images of both the fabricated module and the cooling measurement setup, (c) the measured conversion efficiency η and the maximum output power P_{\max} as a function of temperature difference ΔT with the cold-side temperature T_c as 278 K, (d) the measured maximum temperature difference ΔT_{\max} and the maximum cooling power Q_{\max} as a function of electric current I with the T_h as 323 K, (e) comparison of the conversion efficiency η (at the ΔT of about 95 K) and the measured maximum temperature difference ΔT_{\max} (at the T_h of 323 K) among our fabricated module, SnSe module³², and commercial Bi_2Te_3 module (Zone-melting Bi_2Te_3 data from Deng et al.⁴⁶ and high-performance RC3-8 module type from Marlow Industries, Inc.⁴⁷, respectively. Here it should be noted that since the cooling-performance measurement of SnSe/ Bi_2Te_3 module was performed at the T_h of 300 K, we used the normalized method to calculate the ΔT_{\max} at the T_h of 323 K ($\Delta T_{\max-323\text{K}} = 1.1 \times \Delta T_{\max-300\text{K}}$) for a reasonable comparison, where the multiplying factor 1.1 is obtained based on the data collection from Marlow Industries, Inc.

revealed by Scanning Electron Microscopy (SEM) analysis, the grain size has remarkably increased from several hundred nanometers (sintered at 723 K) to dozens of micrometers (sintered at 1073 K). In addition, the grain morphology has changed from the equiaxed structure (at 723, 873, and 973 K) to the columnar structure (at 1073 K) (Fig. 3), in which the columnar-structure characteristic can be observed in the corresponding low-magnification SEM image (Fig. S4). This is due to the liquid compact sintering effect at the high-temperature that is favorable to the formation of the large and anisotropic grain, as revealed in the previous report⁵¹. Simultaneously, sintering at 1073 K leads to the larger pores size and higher porosity as a direct consequence

of Mg evaporation, whereas sintering at 723 K is unable to realize the dense compact, which can be reflected by the measured sample density (Table S1). Since Mg has a higher saturated vapor pressure than Sb and Bi at a defined temperature, the real chemical composition measured by SEM + EDS proved the Mg loss for sintering at high temperatures (Table S2), consistent with the annealing result of $\text{Mg}_3(\text{Bi}, \text{Sb})_2$ ⁵². Clearly, the pores inside the sample start to appear when the sintering temperature is above 873 K (Fig. S5). In addition, the number of pores, namely the amount of evaporation, is gradually increased with the sintering temperature. However, it is difficult to observe the SPS displacement caused by the Mg evaporation during the sintering

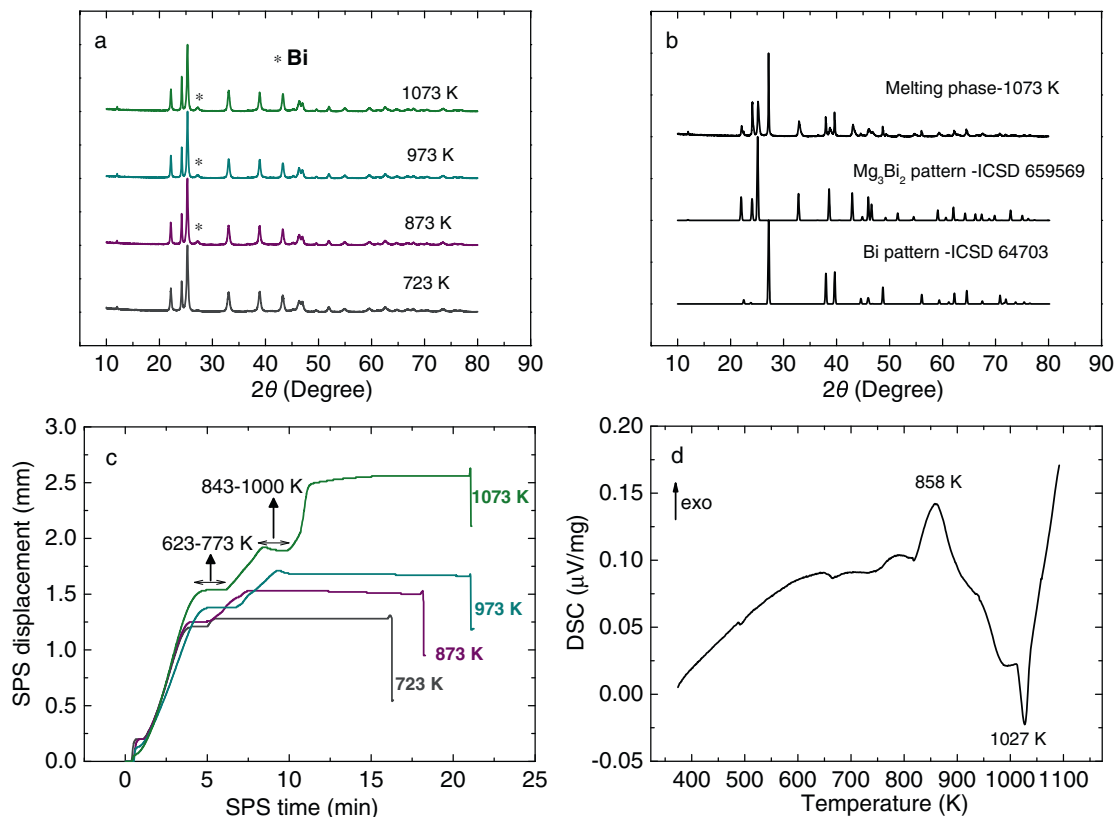


Fig. 2 Phase characterization of $\text{Mg}_{3.2}\text{Bi}_{1.5}\text{Sb}_{0.498}\text{Te}_{0.002}\text{Cu}_{0.01}$ samples at different sintering temperatures (723, 873, 973, and 1073 K). **a** XRD patterns, **(b)** melting-phase XRD pattern of the sample sintered at 1073 K. Here since the XRD pattern position of one melting phase is between Mg_3Bi_2 and Mg_3Sb_2 , the Mg_3Bi_2 pattern is displayed for a simple comparison. **c** Spark plasma sintering (SPS) displacement as a function of sintering time, **(d)** Differential scanning calorimeter (DSC) measurement result of the sample sintered at 723 K.

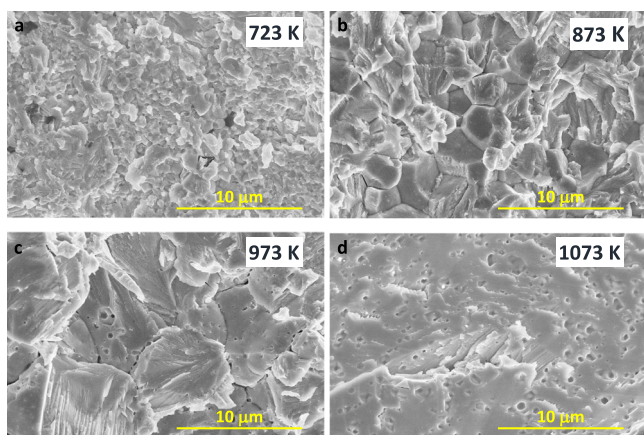


Fig. 3 Microstructural evolution of $\text{Mg}_{3.2}\text{Bi}_{1.5}\text{Sb}_{0.498}\text{Te}_{0.002}\text{Cu}_{0.01}$ samples at different sintering temperatures. **a** 723 K, **(b)** 873 K, **(c)** 973 K, and **(d)** 1073 K.

process since the impact of Mg evaporation is less significant compared to the melting-phase sequent out process.

The microstructural evolution originated from tuning the sintering-temperature effect was illustrated schematically (Fig. 4a). Briefly, sintering at the appropriate temperature realizes the large grain size with small pores and simultaneously minor Cu addition beneficially modifies the grain-boundary complexions with high electrical conductivity³³, both of which contribute to the observed high charge carrier mobility μ_H . A high μ_H around $290 \text{ cm}^2 \text{ V}^{-1} \text{ s}^{-1}$ can be realized in our work through rationally designing the microstructure (Fig. 4b), which is much

higher than these reported Mg_3Bi_2 based samples at the same carrier concentration n_H from Mao et al.²⁵ and Imasato et al.²⁶ It should be noted that at the too-high sintering temperature (\sim at 1073 K), due to both the large pore size and the high porosity, μ_H deteriorates remarkably in turn that was about 22 times less compared to the maximum value. The weighted mobility μ_w is a good tool to assess the potential of the material's electronic properties in thermoelectric^{19,53}, which is independent of the doping element and/or real n_H . Generally, μ_w is codetermined by the drift mobility μ_D and the density of states effective mass m^* , shown in the following equation:

$$\mu_w = \mu_D \left(\frac{m^*}{m_e} \right)^{3/2} \quad (1)$$

where m_e is the electron mass. The calculation method was according to the simplified mathematic model proposed by Zhu et al.⁵⁴ (Table S3). Due to the high μ_H , the sample (sintering at 973 K) possesses the highest μ_w in the $\text{Mg}_3(\text{Bi}, \text{Sb})_2$ system that shares the same tendency with μ_H (Fig. 4c), indicative of the good electronic quality of our synthesized samples.

Tuning the sintering temperature eliminates the thermal grain-boundary resistance and therefore observably reduces the electrical resistivity ρ at the low-temperature range (Fig. 5a). In comparison to these optimized samples from Mao et al. and Imasato et al.^{25,26} our synthesized sample (\sim 973 K) shows the lowest ρ at the whole measured temperature range, due to the combined advantage from tuning the sintering temperature and minor Cu addition. However, the tendency of n_H as a function of sintering temperature is not regular, probably caused by the real-composition change and/or the severe decomposition process at

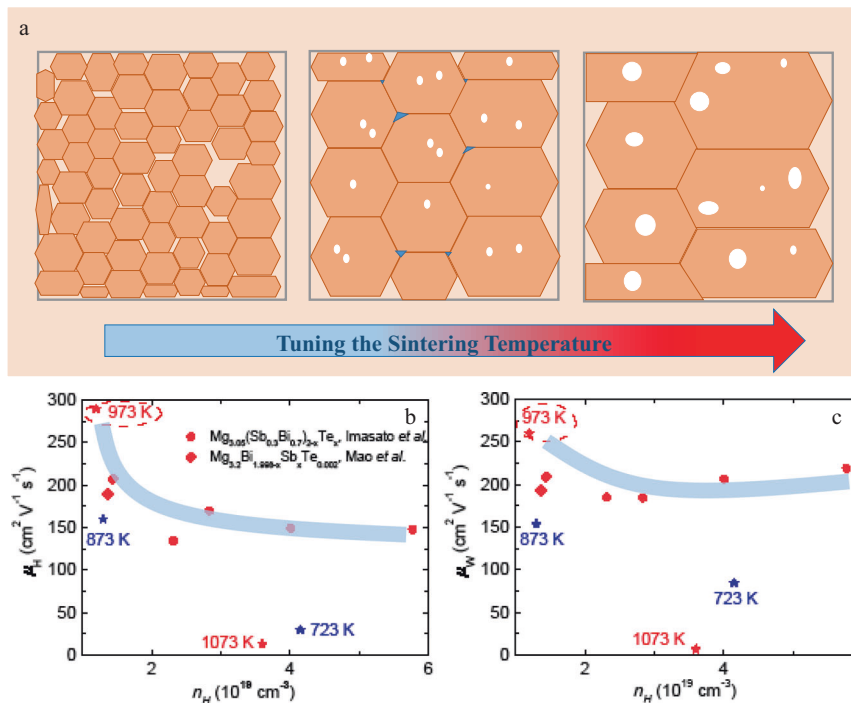


Fig. 4 The effect of tuning the sintering temperature on the electronic properties of $\text{Mg}_{3.2}\text{Bi}_{1.5}\text{Sb}_{0.498}\text{Te}_{0.002}\text{Cu}_{0.01}$ samples. **a** The schematic diagram of microstructural evolution when tuning the sintering temperature, **(b, c)** the measured charge carrier mobility μ_H values and the predicted weighted mobility μ_W as a function of carrier concentration n_H , respectively, in comparison with the data from Mao et al. and Imasato et al.^{25,26}

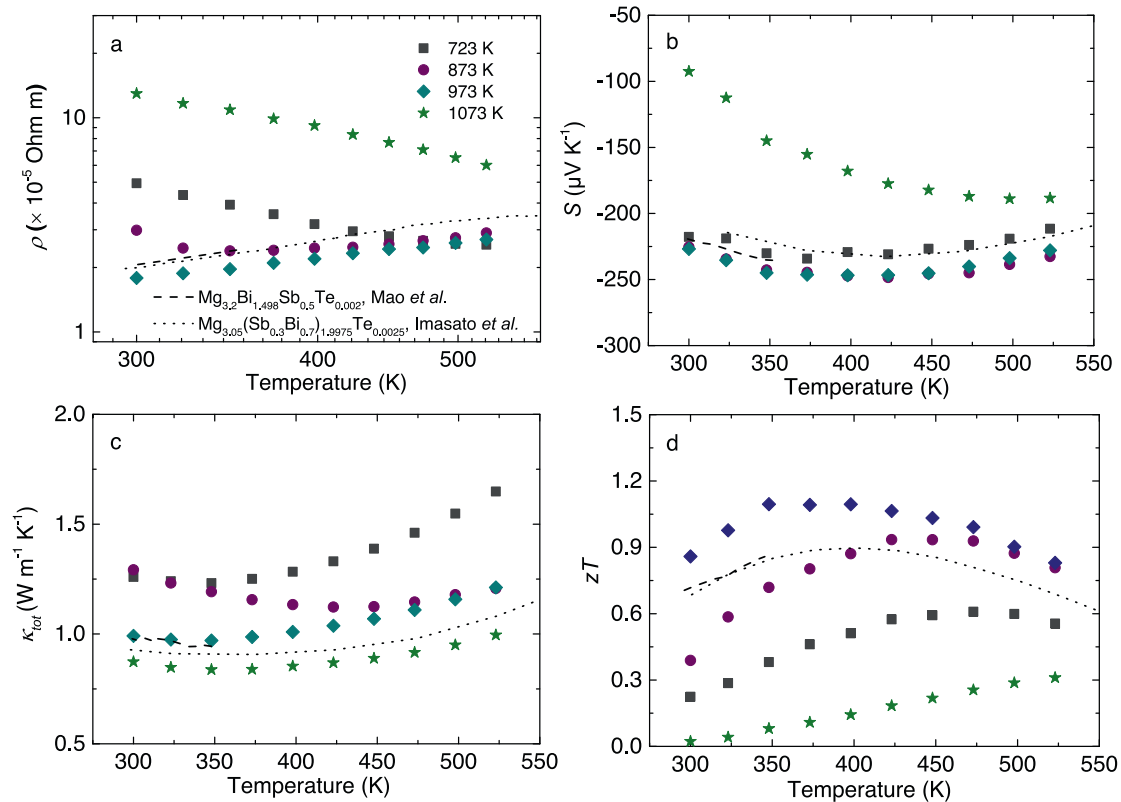


Fig. 5 Temperature-dependent thermoelectric properties of $\text{Mg}_{3.2}\text{Bi}_{1.5}\text{Sb}_{0.498}\text{Te}_{0.002}\text{Cu}_{0.01}$ samples at different sintering temperatures (723, 873, 973, and 1073 K), in comparison to the data from Mao et al. and Imasato et al.^{25,26}. **a-d** Electrical resistivity ρ , Seebeck coefficient S , total thermal conductivity κ_{tot} , and thermoelectric figure of merit zT , respectively.

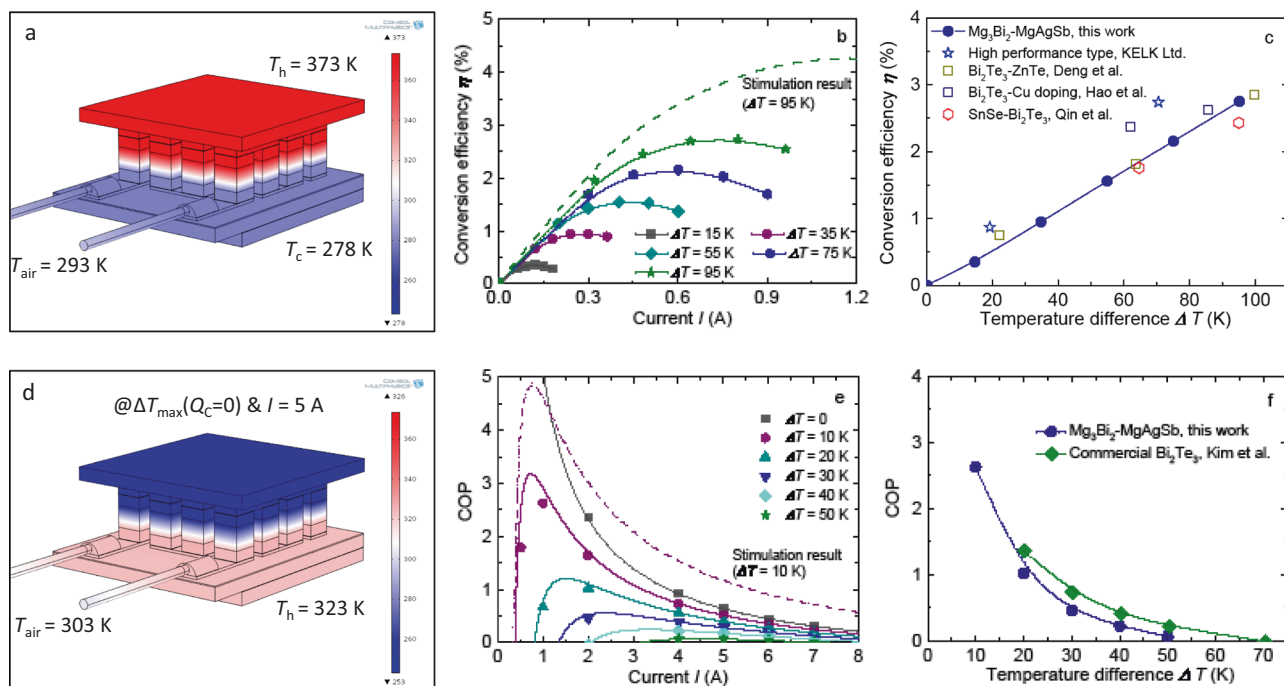


Fig. 6 Thermoelectric performance of our fabricated $\text{Mg}_3\text{Bi}_2\text{-MgAgSb}$ module. **a** Stimulation result of temperature distribution in the fabricated module for power generation using COMSOL Multiphysics® software, **(b)** the measured conversion efficiency η as a function of electric current I at the temperature difference ΔT of 15, 35, 55, 75, and 95 K, **(c)** the measured η as a function of temperature difference ΔT , compared to advanced Bi_2Te_3 modules from research lab^{46,57} and commercial Bi_2Te_3 module from KELK Ltd.⁵⁸, as well as $\text{SnSe-Bi}_2\text{Te}_3$ module³², **(d)** stimulation result of the maximum temperature difference ΔT_{max} in the fabricated module for cooling using COMSOL Multiphysics® software, **(e)** the measured and the predicted COP as a function of electric current I at the temperature difference ΔT of 0, 10, 20, 30, 40, and 50 K, **(f)** comparison of the maximum COP between our fabricated module and commercial Bi_2Te_3 as a function of ΔT .

1073 K. Seebeck coefficient S , however, shows the anomalous tendency (Fig. 5b), irrespective of the ρ or n_H . This is in good agreement with these previous reports in $\text{Mg}_3\text{Sb}_{1.5}\text{Bi}_{0.5}$ ^{55,56}. As a result of the reduced ρ , power factor PF shows a significant enhancement by optimizing the sintering temperature, in which the highest PF in our work surpasses $30 \mu\text{W cm}^{-1} \text{K}^{-2}$ (Fig. S6). Here it should be noted that the obtained S measurement results show some discrepancy between the commercial ZEM-3 and the homemade apparatus in the work of Imasato et al.²⁶ probably due to the cold-finger effect, which may underestimate somewhat the measured PF from Imasato et al.²⁶ Combined with the thermal conductivity κ_{tot} (Fig. 5c), tuning the sintering temperature significantly enhances the thermoelectric figure of merit zT , in which zT above 1 over a broad temperature range from 323 to 423 K is achieved accompanied with a high room-temperature zT close to 0.9 that is the record-high value in the Mg_3Sb_2 system (Fig. 5d).

To further evaluate the potential of our synthesized material for the room-temperature thermoelectric application, an 8-pairs thermoelectric module, consisting of n-type $\text{Mg}_{3.2}\text{Bi}_{1.5}\text{Sb}_{0.498}\text{Te}_{0.002}\text{Cu}_{0.01}$ (sintered at 973 K) and p-type $\alpha\text{-Mg}_{0.99}\text{Cu}_{0.01}\text{Ag}_{0.97}\text{Sb}_{0.99}$, was designed and successfully fabricated. $\alpha\text{-MgAgSb}$, as a high-performance and mechanically robust thermoelectric material, is a promising substitute candidate for p-type (Bi, Sb)₂Te₃²⁴. Cu doping can further optimize thermoelectric properties, leading to a higher average zT (Fig. S7). Concerning the module details, the fabrication method and the corresponding measurement principle, as well as the stimulation theory of theoretical performance were given in the following methods part. First, we performed the three-dimensional finite-element simulations of both power-generation and cooling performance with COMSOL Multiphysics® software in the Heat Transfer Module to optimize the leg geometry and length, shown

in Figs. S8, S9, respectively. The theoretical temperature distribution of our fabricated module is obtained at the hot-side temperature of 373 K (Fig. 6a). Under the optimized I of 0.8 A, the maximum η is 2.8% at the hot-side temperature of 373 K, namely under the temperature difference of 95 K (Fig. 6b). This achieved high η can be comparable to the best Bi_2Te_3 module produced in a research laboratory^{46,57}, but a little lower than the high-performance type commercial module from KELK Ltd⁵⁸ (Fig. 6c). However, the difference between the measured value and theoretical stimulation (dash line in Fig. 6b) is still noticeable. This is primarily due to the larger internal resistance R as a consequence of the relatively large interfacial resistance between the interfacial layer and element material for both n-type and p-type legs, leading to the lower output power P and η in comparison to the theoretical stimulation (Fig. S10). Herein, the interfacial layers of n-type and p-type leg are pure Fe and Ag layers, respectively, both of which do not show the obvious voltage jump around the interface (Fig. S11). Besides, their corresponding EDS mapping images further indicate no observable elemental diffusion (Figs. S12, S13). The interfacial resistance of the present n-type and p-type legs is around $20 \mu\Omega \text{cm}^{-2}$, a little higher than the threshold value of $5 \mu\Omega \text{cm}^{-2}$ accepted for thermoelectric modules with a short leg around 1–2 mm⁵⁹. The resistivity of n-type leg is approximately consistent with that of sample without interfacial layer. However, it is twice larger in p-type leg. The SPS condition must be optimized with elements adding interfacial layer for further improvement. In contrast, the open-circuit voltage V_{oc} and the maximum heat dissipated from the cold side of the module Q_{max} are basically consistent with the simulation results (Fig. S14), which indicates the good accuracy of S and κ measurement, respectively. Regarding thermoelectric cooling, the theoretical cooling temperature difference of our

fabricated module is obtained at the condition of the hot-side temperature of 323 K, air temperature of 303 K, as well as the working current I of 5 A (Fig. 6d). Specifically, one of the most important indexes is the cooling coefficient of performance (COP) that represents the ratio of the amount of heat absorbed Q_C to the total electrical power input P , as $\text{COP} = Q_C/P$. The maximum COP of our fabricated module, under the temperature difference of 10 and 20 K, reaches 2.6 and 1.0 (Fig. 6e), respectively, with the hot-side temperature T_h as 323 K. Importantly, an expected higher COP value, as well as a larger both ΔT_{max} and Q_{max} can be possibly achieved if the contact resistance can be further reduced (Figs. 6e, S15). Our achieved performance can be comparable with the commercial Bi_2Te_3 thermoelectric module (Fig. 6f). The demonstration of remarkably high thermoelectric performance in a non- Bi_2Te_3 module holds great promise for room-temperature power generation and emerging cooling applications.

In summary, we demonstrated the remarkably high thermoelectric performance of non- Bi_2Te_3 module, consisting of n-type $\text{Mg}_3\text{Bi}_{1.5}\text{Sb}_{0.5}$ and p-type $\alpha\text{-MgAgSb}$, for room-temperature power generation and thermoelectric cooling. Herein, the n-type material's thermoelectric performance was maximized through rationally designing the microstructure by tuning the sintering temperature and minor Cu addition. The thermal grain-boundary resistance at the low-temperature range was completely eliminated that contributed to the record-high charge carrier mobility and thus significantly enhanced the electronic properties. Therefore, the achieved room-temperature zT was boosted to 0.9, in addition to a broad temperature plateau above 1 from 323 to 423 K. Our work highlights the importance of microstructure on the charge carrier transport and, more importantly, offers great hope for room-temperature thermoelectric application using non- Bi_2Te_3 materials and devices.

Methods

Materials synthesis. High-purity raw materials from Sigma-Aldrich company were directly weighed according to the nominal composition $\text{Mg}_{3.2}\text{Bi}_{1.5}\text{Sb}_{0.498}\text{Te}_{0.002}\text{Cu}_{0.01}$, as well as $\text{Mg}_{1-x}\text{Cu}_x\text{Ag}_{0.97}\text{Sb}_{0.99}$ ($x = 0$ and 0.01), loaded into the ball-milling jar in the glovebox, and finally subjected to milling process (SPEX SamplePrep 8000 Mixer Mill). The ball-milled powder was directly subjected to sintering without a pre-calcination process. For $\text{Mg}_{3.2}\text{Bi}_{1.5}\text{Sb}_{0.498}\text{Te}_{0.002}\text{Cu}_{0.01}$, the ball-milling time is 5 h and the obtained nanopowders were loaded into the graphite die and sintered by spark plasma sintering (SPS, SPS-1080 System, SPS SYNTEX INC) at different sintering temperatures (723, 873, 973, and 1073 K) with the pressure of ~ 60 MPa for 10 min. For $\text{Mg}_{1-x}\text{Cu}_x\text{Ag}_{0.97}\text{Sb}_{0.99}$, we used the two-step ball-milling method and then did SPS at 573 K^{22,35}.

Phase and microstructure characterizations. The phase structure was characterized by powder X-ray diffraction (XRD, SmartLab3, Rigaku) with Cu K_α radiation. DSC measurement (Netzsch STA 449F1 Jupiter) was performed in an N_2 atmosphere at a heating rate of 15 K/min. The microstructure and composition analysis were characterized using a field emission scanning electron microscope (FESEM, Hitachi S-4800) equipped with an energy dispersive spectrometer (EDS, Horiba EMAXEvolution X-Max).

Material property characterizations. Bar samples with a dimension of around $2.5 \text{ mm} \times 2.5 \text{ mm} \times 9 \text{ mm}$ were cut from the pressed disks and used for simultaneous measurement of electrical resistivity (ρ) and Seebeck coefficient (S) on a commercial system (ULVAC ZEM-3). The thermal conductivity κ_{tot} was calculated using $\kappa_{tot} = DC_p d$, where D , C_p , and d are the thermal diffusivity, specific heat capacity, and density, respectively. The thermal diffusivity coefficient (D) and the specific heat capacity (C_p) were concurrently measured for the disk sample on a laser flash system (Netzsch LFA 467, Germany) with a pyroceram disk as a reference sample. For example, C_p measurement result of $\text{Mg}_{3.2}\text{Bi}_{1.5}\text{Sb}_{0.498}\text{Te}_{0.002}\text{Cu}_{0.01}$ samples sintered at 973 K is in good consistency with the corrected Dulong-Petit law in this material system⁶⁰ (Fig. S15). The sample density (d) was determined by the Archimedes method. The room-temperature Hall coefficient R_H was measured using the PPMS (Physical Properties Measurement System, Quantum Design) with the AC transport option. The data were obtained with a magnetic field sweeping from -5 T to $+5$ T. The Hall carrier concentration (n_H) was

obtained by $n_H = 1/eR_H$ and the Hall carrier mobility (μ_H) was calculated by $\sigma = e\mu_H n_H$, where e is the electronic charge and σ the electrical conductivity. The abovementioned measurement results are directly obtained from one sintering disk.

Module fabrication, performance measurement, and stimulation method.

Thermoelectric legs of n-type $\text{Mg}_{3.2}\text{Bi}_{1.5}\text{Sb}_{0.498}\text{Te}_{0.002}\text{Cu}_{0.01}$ sintered at 973 K and p-type $\text{Mg}_{0.99}\text{Cu}_{0.01}\text{Ag}_{0.97}\text{Sb}_{0.99}$ legs with interfacial layer were fabricated by the one-step SPS using the same condition as previously mentioned. Fe powder and Ag powder for n-type and p-type contact layer was used as the starting material, respectively. These obtained sandwich disks were grinding, polishing, and dicing. The cross-section of legs is $2.0 \text{ mm} \times 2.0 \text{ mm}$ with a total length of 3 mm. The lengths of the thermoelectric elements and interfacial layer are 1.75 mm and 0.8 mm, respectively.

The power-generation performance measurement is similar to previous reports^{33,61}. The eight-couple p- and n-type legs were alternately positioned onto the Cu substrate ($18 \text{ mm} \times 15 \text{ mm} \times 1 \text{ mm}$), where thick Cu patterns were printed onto the heat-conducting polymer film. The legs were interconnected by Cu electrodes, in which InGa eutectic alloy was used for soldering. The power-generation performance was measured in a vacuum on a home-built apparatus with a hot-side temperature of 293, 313, 333, 353, and 373 K, in which the cold-side temperature was fixed at 278 K. The cold-side temperatures T_c and hot-side temperature T_h were measured by using thermocouples embedded in the ceramic plates, respectively. A Cu block with known thermal conductivity (κ_{Cu}) and a fixed cross-sectional area A_{Cu} was used to measure the heat flow. The heat flow out from the cold-side (Q_{out}) was calculated based on Fourier's law:

$$Q_{out} = \kappa_{Cu} \Delta T (A_{Cu}/L_{Pt}) \quad (2)$$

where L_{Pt} is the vertical distance of Pt resistance thermometer in the Cu block and ΔT is the temperature difference along the direction of heat flow. The conversion efficiency η was calculated using the following equation:

$$\eta = \frac{P}{P + Q_{out}} \quad (3)$$

where P is the electrical power output measured by a direct current electronic load.

The cooling-performance fabricated modules were measured keeping a hot-side temperature to be 373 K in a vacuum (10^{-2} – 10^{-3} Pa) on a home-built testing system. The setup is similar with that for power-generation measurement except that hot- and cold-side is upside down and that the Cu block for evaluating heat flow is located above the module.

The three-dimensional finite-element simulations of power-generation and cooling performance was performed with COMSOL Multiphysics[®] software in the Heat Transfer Module. A geometrical model was built in the software interface to represent module with an identical geometry and dimension. The module structure from top to bottom is AlN ceramic 1 mm, graphite foil 0.1 mm, InGa layer 0.03 mm, thermoelectric element 3.35 mm, InGa layer 0.03 mm, Cu foil 0.21 mm, insulation foil 0.08 mm, grease 0.03 mm, and AlN ceramic 1 mm. Herein, the electrical and thermal contact resistances between these interfaces, as well as resistances of Cu electrodes are not considered in our simulation model. The measured temperature-dependent thermoelectric properties of n-type $\text{Mg}_{3.2}\text{Bi}_{1.5}\text{Sb}_{0.498}\text{Te}_{0.002}\text{Cu}_{0.01}$ and p-type $\text{Mg}_{0.99}\text{Cu}_{0.01}\text{Ag}_{0.97}\text{Sb}_{0.99}$ were used for simulation, while those for the Ag and Fe contact layers were assumed to be constant.

Reporting summary. Further information on research design is available in the Nature Research Reporting Summary linked to this article.

Data availability

The data that support the findings of this study are available from the corresponding author upon reasonable request.

Received: 18 December 2021; Accepted: 14 February 2022;

Published online: 02 March 2022

References

1. Chu, S., Cui, Y. & Liu, N. The path towards sustainable energy. *Nat. Mater.* **16**, 16–22 (2017).
2. DiSalvo, F. J. Thermoelectric cooling and power generation. *Science* **285**, 703–706 (1999).
3. Mao, J., Chen, G. & Ren, Z. Thermoelectric cooling materials. *Nat. Mater.* **20**, 454–461 (2021).
4. Nandihalli, N., Liu, C.-J. & Mori, T. Polymer based thermoelectric nanocomposite materials and devices: Fabrication and characteristics. *Nano Energy* **78**, 105186 (2020).
5. Zhang, Q. H. et al. Thermoelectric devices for power generation: recent progress and future challenges. *Adv. Eng. Mater.* **18**, 194–213 (2016).

6. Petsagkourakis, I. et al. Thermoelectric materials and applications for energy harvesting power generation. *Sci. Technol. Adv. Mater.* **19**, 836–862 (2018).
7. Tarancón, A. Powering the IoT revolution with heat. *Nat. Electron.* **2**, 270–271 (2019).
8. Snyder, G. J. & Toberer, E. S. Complex thermoelectric materials. *Nat. Mater.* **7**, 105–114 (2008).
9. Zhu, T. J. et al. Compromise and synergy in high-efficiency thermoelectric materials. *Adv. Mater.* **29**, 1605884 (2017).
10. Pei, Y. Z. et al. Convergence of electronic bands for high performance bulk thermoelectrics. *Nature* **473**, 66–69 (2011).
11. Liu, W. et al. Convergence of conduction bands as a means of enhancing thermoelectric performance of n-type Mg₂Si_{1-x}Snx solid solutions. *Phys. Rev. Lett.* **108**, 166601 (2012).
12. Zhang, J. W. et al. High-performance pseudocubic thermoelectric materials from non-cubic chalcopyrite compounds. *Adv. Mater.* **26**, 3848–3853 (2014).
13. Poudel, B. et al. High-thermoelectric performance of nanostructured bismuth antimony telluride bulk alloys. *Science* **320**, 634–638 (2008).
14. Biswas, K. et al. High-performance bulk thermoelectrics with all-scale hierarchical architectures. *Nature* **489**, 414–418 (2012).
15. Liu, Z. H., Mao, J., Liu, T.-H., Chen, G. & Ren, Z. F. Nano-microstructural control of phonon engineering for thermoelectric energy harvesting. *MRS Bull.* **43**, 181–186 (2018).
16. Mori, T. Novel principles and nanostructuring methods for enhanced thermoelectrics. *Small* **13**, 1702013-n/a (2017).
17. Kuo, J. J. et al. Grain boundary dominated charge transport in Mg₃Sb₂-based compounds. *Energy Environ. Sci.* **11**, 429–434 (2018).
18. Qiu, Q. et al. Grain Boundary Scattering of Charge Transport in n-Type (Hf,Zr)CoSb Half-Heusler Thermoelectric Materials. *Adv. Energy Mater.* **9**, 1803447 (2019).
19. Slade, T. J. et al. Understanding the thermally activated charge transport in NaPbmSbQm+2 (Q = S, Se, Te) thermoelectrics: weak dielectric screening leads to grain boundary dominated charge carrier scattering. *Energy Environ. Sci.* **13**, 1509–1518 (2020).
20. Goldsmid, H. J. & Douglas, R. W. The use of semiconductors in thermoelectric refrigeration. *Br. J. Appl. Phys.* **5**, 386 (1954).
21. Goldsmid, H. J. Bismuth telluride and its alloys as materials for thermoelectric generation. *Materials* **7**, 2577–2592 (2014).
22. Zhao, H. Z. et al. High thermoelectric performance of MgAgSb-based materials. *Nano Energy* **7**, 97–103 (2014).
23. Ying, P. J. et al. High Performance α -MgAgSb Thermoelectric Materials for Low Temperature Power Generation. *Chem. Mater.* **27**, 909–913 (2015).
24. Liu, Z. H., Mao, J., Sui, J. H. & Ren, Z. F. High thermoelectric performance of α -MgAgSb for power generation. *Energy Environ. Sci.* **11**, 23–44 (2018).
25. Mao, J. et al. High thermoelectric cooling performance of n-type Mg₃Bi₂-based materials. *Science* **365**, 495–498 (2019).
26. Imasato, K., Kang, S. D. & Snyder, G. J. Exceptional thermoelectric performance in Mg₃Sb_{0.6}Bi_{1.4} for low-grade waste heat recovery. *Energy Environ. Sci.* **12**, 965–971 (2019).
27. Shi, X. et al. Compromise between band structure and phonon scattering in efficient n-Mg₃Sb_{2-x}Bix thermoelectrics. *Mater. Today Phys.* **18**, 100362 (2021).
28. Zhang, J., Song, L. & Iversen, B. B. Insights into the design of thermoelectric Mg₃Sb₂ and its analogs by combining theory and experiment. *npj Comput. Mater.* **5**, 76 (2019).
29. Li, A., Fu, C., Zhao, X. & Zhu, T. High-Performance Mg₃Sb_{2-x}Bix thermoelectrics: progress and perspective. *Research* **2020**, 1934848 (2020).
30. Shang, H. et al. N-Type Mg₃Sb_{2-x}Bix alloys as promising thermoelectric materials. *Research* **2020**, 1219461 (2020).
31. Zhao, L.-D. et al. Ultrahigh power factor and thermoelectric performance in hole-doped single-crystal SnSe. *Science* **351**, 141–144 (2016).
32. Qin, B. et al. Power generation and thermoelectric cooling enabled by momentum and energy multiband alignments. *Science* **373**, 556–561 (2021).
33. Liu, Z. H. et al. Demonstration of ultrahigh thermoelectric efficiency of ~7.3% in Mg₃Sb₂/MgAgSb module for low-temperature energy harvesting. *Joule* **5**, 1196–1208 (2021).
34. Ying, P. et al. Towards tellurium-free thermoelectric modules for power generation from low-grade heat. *Nat. Commun.* **12**, 1121 (2021).
35. Liu, Z. H. et al. Lithium doping to enhance thermoelectric performance of MgAgSb with weak electron-phonon coupling. *Adv. Energy Mater.* **6**, 1502269 (2016).
36. Tamaki, H., Sato, H. K. & Kanno, T. Isotropic conduction network and defect chemistry in Mg_{3+ δ} Sb_{2- δ} based layered Zintl compounds with high thermoelectric performance. *Adv. Mater.* **28**, 10182–10187 (2016).
37. Zhang, J. et al. Discovery of high-performance low-cost n-type Mg₃Sb₂-based thermoelectric materials with multi-valley conduction bands. *Nat. Commun.* **8**, 13901 (2017).
38. Shuai, J. et al. Tuning the carrier scattering mechanism to effectively improve the thermoelectric properties. *Energy Environ. Sci.* **10**, 799–807 (2017).
39. Chen, X. X. et al. Extraordinary thermoelectric performance in n-type manganese doped Mg₃Sb₂ Zintl: High band degeneracy, tuned carrier scattering mechanism and hierarchical microstructure. *Nano Energy* **52**, 246–255 (2018).
40. Shu, R. et al. Mg₃+ δ Sb_xBi_{2-x} family: a promising substitute for the state-of-the-art n-Type thermoelectric materials near room temperature. *Adv. Funct. Mater.* **29**, 1807235 (2019).
41. Shi, X. et al. Extraordinary n-type Mg₃SbBi thermoelectrics enabled by Yttrium doping. *Adv. Mater.* **31**, 1903387 (2019).
42. Zhang, J. & Iversen, B. B. Fermi surface complexity, effective mass, and conduction band alignment in n-type thermoelectric Mg₃Sb_{2-x}Bix from first principles calculations. *J. Appl. Phys.* **126**, 085104 (2019).
43. Zhang, F. et al. High-performance N-type Mg₃Sb₂ towards thermoelectric application near room temperature. *Adv. Funct. Mater.* **30**, 1906143 (2020).
44. Liang, Z. et al. High thermoelectric energy conversion efficiency of a unicolor of n-type Mg₃Bi₂ and p-type Bi₂Te₃. *Mater. Today Phys.* **19**, 100413 (2021).
45. Chen, X. et al. Excellent thermoelectric performance of boron-doped n-type Mg₃Sb₂-based materials via the manipulation of grain boundary scattering and control of Mg content. *Sci. China Mater.* **64**, 1761–1769 (2021).
46. Deng, R. et al. High thermoelectric performance in Bi_{0.46}Sb_{1.54}Te₃ nanostructured with ZnTe. *Energy Environ. Sci.* **11**, 1520–1535 (2018).
47. Marlow I. V. Thermoelectric generator (TEG) modules. <https://ii-vi.com/product/thermoelectric-generator-teg-modules/> (2021).
48. Diouf, S. & Molinari, A. Densification mechanisms in spark plasma sintering: effect of particle size and pressure. *Powder Technol.* **221**, 220–227 (2012).
49. Cai, B. et al. Spark plasma sintered Bi-Sb-Te alloys derived from ingot scrap: maximizing thermoelectric performance by tailoring their composition and optimizing sintering time. *Nano Energy* **85**, 106040 (2021).
50. Jørgensen, L. R., Zhang, J., Zeuthen, C. B. & Iversen, B. B. Thermal stability of Mg₃Sb_{1.475}Bi_{0.475}Te_{0.05} high performance n-type thermoelectric investigated through powder X-ray diffraction and pair distribution function analysis. *J. Mater. Chem. A* **6**, 17171–17176 (2018).
51. Song, H. & Coble, R. L. Origin and growth kinetics of platelike abnormal grains in liquid-phase-sintered alumina. *J. Am. Ceram. Soc.* **73**, 2077–2085 (1990).
52. Shang, H. et al. N-type Mg₃Sb_{2-x}Bix with improved thermal stability for thermoelectric power generation. *Acta Mater.* **201**, 572–579 (2020).
53. Wang H., Pei Y., LaLonde A. D. & Snyder G. J. In *Thermoelectric Nanomaterials* (eds Koumoto, K. & Mori, T.). (Springer, Berlin, Heidelberg, 2013).
54. Zhu, J. et al. Restructured single parabolic band model for quick analysis in thermoelectricity. *npj Comput. Mater.* **7**, 116 (2021).
55. Kanno, T. et al. Enhancement of average thermoelectric figure of merit by increasing the grain-size of Mg₃. 2Sb₁. 5Bi₀. 49Te₀. 01. *Appl. Phys. Lett.* **112**, 033903 (2018).
56. Mao, J. et al. Defect Engineering for realizing high thermoelectric performance in n-type Mg₃Sb₂-based materials. *ACS Energy Lett.* **2**, 2245–2250 (2017).
57. Hao, F. et al. High efficiency Bi₂Te₃-based materials and devices for thermoelectric power generation between 100 and 300 °C. *Energy Environ. Sci.* **9**, 3120–3127 (2016).
58. Ltd., K. High performance type/multi purpose type. https://www.kelk.co.jp/products/data_1.html#data_1_1 (2019).
59. Liu, W. & Bai, S. Thermoelectric interface materials: a perspective to the challenge of thermoelectric power generation module. *J. Materiomics* **5**, 321–336 (2019).
60. Agne, M. T. et al. Heat capacity of Mg₃Sb₂, Mg₃Bi₂, and their alloys at high temperature. *Mater. Today Phys.* **6**, 83–88 (2018).
61. Hu, X. et al. Power generation from nanostructured PbTe-based thermoelectrics: comprehensive development from materials to modules. *Energy Environ. Sci.* **9**, 517–529 (2016).

Acknowledgements

This work was supported by JST Mirai Program Grant Number JPMJMI19A1 by T.M. C.H.L. thanks JST CREST grant number JPMJCR20Q4 for funding.

Author contributions

Z.L., W.G., H.O., K.N., C.H.L., and T.M. designed the work. Z.L. and W.G. synthesized the samples, performed the microstructural characterization, and measured the performance. H.O., K.N., and C.H.L. fabricated the module, measured the module performance, and performed the stimulation. Z.L., W.G., and T.M. wrote the paper. All authors edited the paper.

Competing interests

Two Japanese patent applications (2020-151704 and 2020-155093) and two WIPO PCT patent applications (JP2021/031105 and JP2021/031156) were filed by T.M. and Z.L. The remaining authors declare no competing interests.

Additional information

Supplementary information The online version contains supplementary material available at <https://doi.org/10.1038/s41467-022-28798-4>.

Correspondence and requests for materials should be addressed to Takao Mori.

Peer review information *Nature Communications* thanks Tsutomu Kanno and the other anonymous reviewer(s) for their contribution to the peer review of this work. Peer reviewer reports are available.

Reprints and permission information is available at <http://www.nature.com/reprints>

Publisher's note Springer Nature remains neutral with regard to jurisdictional claims in published maps and institutional affiliations.



Open Access This article is licensed under a Creative Commons Attribution 4.0 International License, which permits use, sharing, adaptation, distribution and reproduction in any medium or format, as long as you give appropriate credit to the original author(s) and the source, provide a link to the Creative Commons license, and indicate if changes were made. The images or other third party material in this article are included in the article's Creative Commons license, unless indicated otherwise in a credit line to the material. If material is not included in the article's Creative Commons license and your intended use is not permitted by statutory regulation or exceeds the permitted use, you will need to obtain permission directly from the copyright holder. To view a copy of this license, visit <http://creativecommons.org/licenses/by/4.0/>.

© The Author(s) 2022